Theoretical study of the response of 12 cubic metals to uniaxial loading

Frederick Milstein and Somchart Chantasiriwan*
Departments of Materials and Mechanical Engineering, University of California, Santa Barbara, California 93106
(Received 7 October 1997; revised manuscript received 30 March 1998)

The theoretical mechanical response of 12 cubic metals (Al, Cu, Mo, Na, Li, K, Rb, Nb, Fe, Ni, Au, and Ag) to unconstrained uniaxial loadings, coaxial with each of the three principal symmetry directions, is analyzed, at finite strain, in the framework of the embedded-atom method model calculations. The models have been formulated to reproduce, identically, empirical values of the three second-order elastic moduli (C_{11}, C_{12}, and C_{44}) and the six third-order elastic moduli (C_{111}, C_{112}, C_{123}, C_{144}, C_{166}, and C_{456}), and thus both the linear (harmonic) and nonlinear (anharmonic) response of the metals is represented in the computations. The mechanical behavior, including theoretical strengths, is strongly influenced by crystalline symmetries and bifurcation phenomena. Characteristic anisotropies, both at infinitesimal and at finite strain, are associated with each of three subgroups, i.e., the fcc metals, the bcc alkali metals, and the bcc group-V and group-VI transition metals. The behavior of bcc Fe is intermediate to that of the bcc alkalis and that of the group-V and group-VI transition metals. For the fcc metals under [100] loading, the maximum stress generally is about 20–50 % of the value of Young's modulus, although a potential instability associated with the vanishing of the elastic moduli combination $C_{22}-C_{23}$ occurs at stresses of about 10–25 % of Young's modulus. Also, for the fcc metals, the maximum tensile stress in [111] loading is generally comparable with that in [100] loading, but in [110] loading, the maximum stresses are only about 2–5 % of the respective Young's modulus values. By contrast, in the bcc alkali metals, the maximum tensile stress in [100] loading is only about 1–3 % of Young's modulus, while in [111] and [110] loading, these percentages are about 10% and 30–35 %, respectively. The relative anisotropy of the bcc transition metals at finite strain is much less than that of the bcc alkali metals. For example, the maximum theoretical stresses in Nb range from about 25 GPa (in [100] loading) to 70 GPa (in [111] loading); for bcc Na, these values range from about 0.04 GPa (in [100] loading) to 2 GPa (in [110] loading). [S0163-1829(98)00730-9]

I. INTRODUCTION

The study of solids under hydrostatic pressure has long been an active field of research.[1] In recent years, interest in homogeneous, large strain, nonhydrostatic deformation of crystals has accelerated; see, e.g., Refs. 2–6, and the citations therein. With a view toward the development of models for use in theoretical, finite strain, studies, Chantasiriwan and Milstein[7] developed a technique for incorporating experimental values of the second-order elastic moduli (SOEM) and third-order elastic moduli (TOEM) in models of cubic metals described by the embedded-atom method (EAM).[8] In the preceding paper,[9] this technique is used to construct specific EAM models for 12 metals, viz, Al, Cu, Mo, Na, Li, K, Rb, Nb, Fe, Ni, Au, and Ag. The models identically reproduce empirical values of the three SOEM (C_{11}, C_{12}, and C_{44}) and six TOEM (C_{111}, C_{112}, C_{123}, C_{144}, C_{166}, and C_{456}) of the respective metals. Additionally they yield theoretical pressure-volume curves and phonon-dispersion relations that are generally in good agreement with experiment. The present paper examines the theoretical response of these models to unconstrained uniaxial loading along each of the three principal symmetry directions of a cubic crystal, i.e., [100], [110], and [111]. The loading is ''unconstrained uniaxial'' in the sense that, at each stage, on each of the loading paths, the lattice parameters that are transverse to the direction of load are allowed to ''relax,'' by an iteration technique, to the state where the transverse loads vanish. Since the models incorporate empirical values of the SOEM and TOEM, both the linear (harmonic) and nonlinear (anharmonic) elastic response of the metals may be presumed to be reasonably accurately reproduced by the model calculations.

A number of years ago, Hill[10] observed that ''Single crystals free from lattice imperfections are used increasingly as microstructural components. Perfect crystals are capable of elastic strains well beyond what can properly be treated as infinitesimal. Their response to general loading is virtually unknown and is doubtless complex ... .'' Atomistic model computations can shed light on these complexities, particularly when comprehensive comparisons are made among different metals, crystal structures, and loading directions. Such comparisons can also serve to distinguish between finite strain responses that are sensitive to specific *details* of atomic binding and those dependent mainly on just crystal symmetries and the *general* nature of interatomic forces, i.e., attractive between atoms at relatively large interatomic spacing and repulsive between close, neighboring atoms.

Milstein and co-workers[11–13] have analyzed the infinitesimal elastic response of cubic crystals to uniaxial loading, based on the general nature of interatomic forces, on crystalline symmetries, and on theoretical bifurcations occurring at finite strain. They deduced ''standard models'' for fcc and bcc crystals. In the standard model of an fcc crystal,[11,12] (i) the initial values of Young's modulus are ordered according to $E_{111}>E_{110}>E_{100}$ (the subscripts indicate the crystallographic direction of loading), (ii) a concave downward curvature occurs in the initial portion of the stress-strain curve in [111] and [110] uniaxial loading and a concave upward

curvature in [100] loading, and (iii) Poisson's ratio $\nu_{110}^{1\bar{1}0}$ is negative.[11,14] (For a crystal loaded uniaxially in the $[hkl]$ direction, Poisson's ratio $\nu_{hkl}^{h'k'l'} \equiv -\varepsilon_{h'k'l'}/\varepsilon_{hkl}$, where ε_{hkl} and $\varepsilon_{h'k'l'}$ are, respectively, the axial and transverse strains; the superscript on ν is omitted if the transverse strain is isotropic.) There is generally good agreement between this ''standard'' model of fcc crystals and experimental observation;[11,12,14] the only apparent exceptions are Al (for which $\nu_{110}^{1\bar{1}0}>0$ and the [100] loading curve is initially concave downward), Pt and Ir ($\nu_{110}^{1\bar{1}0}>0$), and Pd ($\nu_{110}^{1\bar{1}0}<0$ except at low temperatures).

According to experimental data and pseudopotential computations,[13] the alkali metals and various β brasses behave, as a group, in agreement with the standard model of a bcc crystal, in which (i) Young's moduli are ordered according to $E_{111}>E_{110}>E_{100}$, (ii) the initial portion of the stress-strain curve is concave downwards in [100] and [111] loading but concave upwards in [110] loading, and (iii) Poisson's ratio $\nu_{110}^{1\bar{1}0}$ is negative. On the other hand, the experimentally determined elastic properties of the bcc group-V transition metals V and Nb and the group-VI transition metals Cr, Mo, and W are not consonant with the standard model of a bcc crystal; for these metals, $\nu_{110}^{1\bar{1}0}$ is positive and the ordering of Young's moduli is reversed, i.e., $E_{100}>E_{110}>E_{111}$. To our knowledge, no previous model computations of the uniaxial loading behavior, at finite strain, have been carried out on crystals with this characteristic infinitesimal response. Other relations and orderings among Young's moduli, the shear moduli, and Poisson's ratios are discussed in Ref. 15, and stability and bifurcation principles are presented in Refs. 16–18.

II. COMPUTATIONAL PROCEDURE

Consider a cubic crystal as it is deformed homogeneously under uniaxial load along any one of its three principal symmetry directions. The stretch λ_α of any fiber is defined as its length in the current state divided by its initial length (in the reference, or unstressed, cubic state); the terms ''stretch'' and ''strain'' are used interchangeably although, strictly speaking, strain may be defined as $\lambda_\alpha - 1$. The stretch coaxial with the applied load is λ_a; under [100] and [111] loading, the transverse stretch λ_t is isotropic; under [110] loading, the transverse stretches in the [001] and [110] directions are designated as λ_t^{001} and $\lambda_t^{1\bar{1}0}$, respectively. The crystal structure on each of the primary loading paths may be described in terms of a crystallographic cell, called the ''computational cell,'' the edges of which are formed by three mutually orthogonal vectors $\mathbf{a}_1$, $\mathbf{a}_2$, and $\mathbf{a}_3$. The computational cell is unique to the particular structure and mode of loading; in the unstressed state, the computational cell is identical to the conventional cubic cell only for the [100] modes of loading. The vectors $\mathbf{a}_i$ may be expressed in terms of a fixed frame of reference that has mutually orthogonal unit vectors $\hat{i}$, $\hat{j}$, and $\hat{k}$. These unit vectors are parallel to the edges of the initial (unstressed), conventional, cubic cell, which may be either face-centered or body-centered cubic; the unstressed lattice parameter, or cube edge, of this cell is a^0.

With the direction of load defined parallel to $\mathbf{a}_1$, the edges of the computational cell may be expressed in terms of the stretches and unit vectors. For [100] loading of structures that are initially bcc or fcc,

$$\mathbf{a}_1=\lambda_a a^0\hat{i}, \quad \mathbf{a}_2=\lambda_t a^0\hat{j}, \quad \mathbf{a}_3=\lambda_t a^0\hat{k}. \tag{1}$$

The initial computational cells are thus cubic; under load they are tetragonal. For [110] loading of an initial bcc structure,

$$\mathbf{a}_1=\lambda_a a^0(\hat{i}+\hat{j}), \quad \mathbf{a}_2=\lambda_t^{1\bar{1}0} a^0(-\hat{i}+\hat{j}), \quad \mathbf{a}_3=\lambda_t^{001} a^0\hat{k}. \tag{2a}$$

The computational cell is face-centered tetragonal initially, and it becomes face-centered orthorhombic under load. For [110] loading of an initial fcc crystal,

$$\mathbf{a}_1=\frac{\lambda_a a^0}{2}(\hat{i}+\hat{j}), \quad \mathbf{a}_2=\frac{\lambda_t^{1\bar{1}0} a^0}{2}(-\hat{i}+\hat{j}), \quad \mathbf{a}_3=\lambda_t^{001} a^0\hat{k}. \tag{2b}$$

The computational cell is initially body-centered tetragonal, and it becomes body-centered orthorhombic under load. Finally, under [111] loading,

$$\mathbf{a}_1=\frac{\lambda_a a^0}{2}(\hat{i}+\hat{j}+\hat{k}), \quad \mathbf{a}_2=\lambda_t a^0(-2\hat{i}+\hat{j}+\hat{k}),$$

$$\mathbf{a}_3=\lambda_t a^0(-\hat{j}+\hat{k}) \tag{3a}$$

for the bcc crystal, and

$$\mathbf{a}_1=\lambda_a a^0(\hat{i}+\hat{j}+\hat{k}), \quad \mathbf{a}_2=\frac{\lambda_t a^0}{2}(-2\hat{i}+\hat{j}+\hat{k}),$$

$$\mathbf{a}_3=\frac{\lambda_t a^0}{2}(-\hat{j}+\hat{k}) \tag{3b}$$

for fcc. The crystal structure is trigonal under [111] loading, although the computational cell is orthorhombic.

The energy per atom E of a homogeneously deformed cubic crystal may be expressed as a function of six geometric parameters, which we take as the lengths of the edges a_1, a_2, and a_3 of the computational cell and their included angles, a_4, a_5, and a_6. With this designation, in the EAM,

$$E(a_1,a_2,a_3,a_4,a_5,a_6)=F(\rho)+\tfrac{1}{2}\sum_l \phi(r_l), \tag{4a}$$

with

$$\rho=\sum_l f(r_l), \tag{4b}$$

where r_l is the distance between the atom at the lth site and the atom at the origin; the index l is summed over all sites except the origin. The explicit pair-potential functions $\phi(r)$ and electron-density functions $f(r)$ used in the present study are given by Eqs. (2) and (3) in Ref. 9; the corresponding model parameters are listed in Ref. 9, Table II. The embedding function $F(\rho)$ is determined from a modification of Rose's equation of state; see Eqs. (9)–(12) of Ref. 9.

The vector connecting the atom at the origin and the atom at the lth atomic site may be written as

$$\mathbf{r}_l=\tfrac{1}{2}(l_1\mathbf{a}_1+l_2\mathbf{a}_2+l_3\mathbf{a}_3), \tag{5}$$

where (for a given initial crystal structure and mode of loading) l_1, l_2, and l_3 are numerical indices that are unique to the particular site l. For a crystal under load, specification of all allowed sets of indices, l_1, l_2, l_3, and the vectors forming the edges of the computational cell, $\mathbf{a}_1$, $\mathbf{a}_2$, and $\mathbf{a}_3$, also completely determines the crystal structure. In practice, a computer algorithm selects the sets of l_1, l_2, l_3 that are appropriate to the particular structure and mode of loading under consideration. For [100] loading of bcc crystals and [110] loading of fcc crystals, the computational cells are body centered, and the lattice summations are over all sets of integer values l_1, l_2, l_3, subject to the restriction that l_1, l_2, and l_3 are either all even or all odd integers at any given site l. Under [100] loading of fcc crystals and [110] loading of bcc crystals, the computational cells are face centered, and l_1, l_2, and l_3 take on all integer values, subject to the restriction that $l_1+l_2+l_3$ is an even integer. Under [111] loading of either the bcc or fcc structure, all sites l are included that satisfy the conditions $(l_1,l_2,l_3)=(m_1,m_2,m_3)$ or $(m_1\pm\frac{2}{3},m_2\mp\frac{2}{3},m_3)$, where m_1, m_2, and m_3 are integers, with the restriction that m_1 and m_2+m_3 are even, or equivalently, $(l_1,l_2,l_3)=(2n_1,n_2,2n_3-n_2)$ or $(2n_1\pm\frac{2}{3},n_2\mp\frac{2}{3},2n_3-n_2)$, where n_1, n_2, and n_3 comprise all sets of integers.

The axial load per unit reference area L_i, coaxial with $\mathbf{a}_i$ and normal to the j-k face of the computational cell is

$$L_i=\frac{N}{a_j^0a_k^0}\frac{\partial E}{\partial a_i}=\frac{a_i^0}{V^0}\frac{\partial E}{\partial a_i},\quad i=1,2,3,\quad i\neq j\neq k; \tag{6}$$

N is the number of atoms per computational cell (two for bcc under [100] and fcc under [110] loadings, four for fcc under [100] and bcc under [110] loadings, and six for both structures under [111] loading); V^0 is the volume per atom in the unstressed cubic state, and a_i^0 is the length of the ith edge of the computational cell in this state. The axial loads divided by the current cross-sectional areas on which they act (i.e., the ''true stresses'') are

$$\sigma_i=\frac{N}{a_ja_k}\frac{\partial E}{\partial a_i}=\frac{a_i}{V}\frac{\partial E}{\partial a_i},\quad i=1,2,3,\quad i\neq j\neq k; \tag{7}$$

V is the current volume per atom. The crystalline symmetry on the uniaxial loading paths ensures that no shear stresses act on the faces of the computational cell. In the EAM,

$$\frac{\partial E}{\partial a_i}=F'\sum f'\frac{\partial r^2}{\partial a_i}+\frac{1}{2}\sum\phi'\frac{\partial r^2}{\partial a_i}, \tag{8}$$

where $F'=dF/d\rho$, $f'=df/dr^2$, $\phi'=d\phi/dr^2$, and $d/dr^2=(1/2r)(d/dr)$. Also, from Eq. (5),

$$r^2=\tfrac{1}{4}(l_1^2a_1^2+l_2^2a_2^2+l_3^2a_3^2+2l_2a_2l_3a_3\cos a_4 +2l_1a_1l_3a_3\cos a_5+2l_1a_1l_2a_2\cos a_6); \tag{9}$$

so, for $i=1$, 2, or 3, $\partial r^2/\partial a_i=a_il_i^2/2$ and

$$\frac{\partial E}{\partial a_i}=\frac{a_i}{2}F'\sum f'l_i^2+\frac{a_i}{4}\sum\phi'l_i^2, \tag{10}$$

when $a_4=a_5=a_6=90°$. The axial loads and stresses are readily computed with the aid of Eqs. (6)–(10). At each stage of loading (i.e., for each selected value of the lattice parameter a_1), an iteration procedure is used to determine the values of a_2 and a_3 that render $\partial E/\partial a_2=\partial E/\partial a_3=0$ to within the required numerical accuracy. This procedure thus locates the states of uniaxial loading, at which the ''final'' transverse stretches are recorded and the uniaxial loads L_a and stresses σ_a are computed, as functions of axial stretch λ_a.

The main concern of the present paper is the ''stress-strain'' response of the crystals on their primary loading paths. Another important consideration, which shall be dealt with extensively, in due course, is stability under load. Here we also determine the locations of a particularly interesting potential instability, associated with the vanishing of the moduli combination $C_{22}-C_{23}$, under [100] uniaxial load. Elastic moduli are central in theories of branching and instability. For a crystal under load, elastic moduli may be defined in terms of second derivatives of internal energy with respect to some convenient choice of geometric parameters or strain variables q_r, i.e., in terms of $\partial^2E/\partial q_r\partial q_s$. In pioneering work, Born and co-workers[19–21] took the ''positive definiteness'' of the matrix of second-order moduli C_{rs} (the values of which vary with crystal deformation) to be synonymous with stability. This may be expressed as $C_{rs}\delta q_r\delta q_s>0$ (summation convention, $r,s=1,2,...,6$), where δ represents a small, incremental change. However, as first noted by Hill,[10] and elaborated by Hill and Milstein,[16] Born's criterion omits the effects of external loading upon the assessment of stability; specifically it includes first- and second-order internal energy terms, $p_r\delta q_r$ and $C_{rs}\delta q_r\delta q_s$, but neglects second-order work terms, $k_{rs}\delta q_r\delta q_s$, where the k_{rs} represent second derivatives of external work with respect to the strain variables; the k_{rs} depend on test configuration and choice of variables q_r. It follows, in general, that theoretical ''ranges of stability'' computed via Born's criterion depend upon the choice of parameters used to define strain in a crystal under load, and thus such ranges do not represent intrinsic measures of crystal strength or stability (except in special, invariant cases as noted below). Hill and Milstein[16] modified Born's criterion to a coordinate invariant form, $(C_{rs}-k_{rs})\delta q_r\delta q_s>0$, and in subsequent work[22,23] demonstrated the importance, quantitatively, of the k_{rs} terms. There are, however, certain modes of loading and subsequent instability under which both $C_{rs}\delta q_r\delta q_s$ and $(C_{rs}-k_{rs})\delta q_r\delta q_s$ pass from positive definite to indefinite at the same state, independent of the algebraic forms of the q_r. Hill and Milstein[16] have shown the state, where $C_{22}-C_{23}=0$ on a primary path of [100] loading of an initially cubic crystal, to possess this characteristic and hence have termed it the ''invariant $C_{22}=C_{23}$ eigenstate'' (see Ref. 16 for further details). Now consider a crystal subjected to a given mode of loading. On a stable primary path, the crystal's symmetry remains unchanged (e.g., an initially cubic crystal under [100] loading remains tetragonal) and its incremental response to a change in load depends on its current values of *second*-order elastic moduli. At the termination of a stable

range, where $(C_{rs}-k_{rs})\delta q_r \delta q_s > 0$ is first violated for any set δq_r (not all of which are zero), the crystal may branch or bifurcate to a secondary path of lower energy and new symmetry. The nature of this branching may depend not only on the second-order moduli, but also on the *higher*-order moduli at the branch point.[24] For initially cubic crystals, two specific cases have been worked out in detail, i.e., branching from tetragonal to orthorhombic under [100] loading and from cubic to tetragonal under hydrostatic pressure. The former occurs at $C_{22}-C_{23}=0$ (Refs. 5, 17, 18, and 24) and the secondary path characterization at the branch point (i.e., stress σ_a versus stretch λ_a) depends on ''up to'' fourth-order moduli C_{rstu} at the point where $C_{22}-C_{23}=0$. The latter (i.e., branching from cubic to tetragonal) occurs at the hydrostatic pressure where the shear modulus μ vanishes and depends on ''up to'' third-order moduli C_{rst}.[25]

The state where $C_{22}-C_{23}=0$ on the [100] loading path is interesting for a variety of reasons. First, as mentioned above, its location on the primary loading path is independent of the choice of geometric variables q_r (provided, of course, that q_1 is coaxial with the loading direction and q_2 and q_3 are coincident with the transverse crystal axes, $\mathbf{a}_2$ and $\mathbf{a}_3$). Second, branching occurs under dead load,[10,16] from the tetragonal structure to an orthohombic structure,[17,18] thus forming a secondary loading path, of an orthorhombic crystal structure, under uniaxial load. In prior computations with both pseudopotential and Morse models of elastically stable fcc (or bcc) crystals, after the $C_{22}=C_{23}$ state is reached, the uniaxial load drops (or increases) rapidly, through zero, on the secondary path as λ_a increases (or decreases) under continued longitudinal extension of the initially fcc crystal (or under continued longitudinal compression of the initially bcc crystal).[5,17,18] In this region the crystals were unstable, owing to the negative slope of the σ_a versus λ_a path, so the $C_{22}=C_{23}$ eigenstate has been found to limit the theoretical strength of fcc crystals in [100] uniaxial tension (or bcc crystals in [100] uniaxial compression). [The state of ''maximum stress'' or ''maximum theoretical tensile stress'' is reached when the true stress (i.e., load divided by current cross-sectional area) achieves its maximum theoretical value on the primary path, regardless of whether the crystal is stable as this state is approached. The value of stress at this point is often taken as the ''theoretical strength'' of the crystal under the particular mode of loading, although, more accurately, it is an ''upper bound'' to the theoretical strength. If an instability is known to occur at some point on the primary path before the maximum stress is reached, the value of stress at the instability represents a lower ''upper bound'' to the theoretical strength.] Third, the orthorhombic uniaxial loading paths that branch from the [100] path at the $C_{22}=C_{23}$ state also pass through the unstressed cubic configurations, and these secondary paths are in fact the primary paths of [110] loading of cubic crystals. These bifurcations thus profoundly affect the character of the [110] loading paths,[12,13] which, in turn, determines the nature of crack propagation during atomistic simulations[26] of rapidly applied uniaxial loadings. Finally, these bifurcations can be associated with bcc↔fcc transitions in the alkali metals under uniaxial loading.[5,6]

With $q_i \equiv a_i$, moduli C_{ij} are readily computed from

$$\frac{\partial^2 E}{\partial a_i \partial a_j} = \left(F'' \sum f' \frac{\partial r^2}{\partial a_i} \right) \sum f' \frac{\partial r^2}{\partial a_j} + F' \sum f'' \frac{\partial r^2}{\partial a_i} \frac{\partial r^2}{\partial a_j} + F' \sum f' \frac{\partial^2 r^2}{\partial a_i \partial a_j} + \frac{1}{2} \sum \phi'' \frac{\partial r^2}{\partial a_i} \frac{\partial r^2}{\partial a_j} + \frac{1}{2} \sum \phi' \frac{\partial^2 r^2}{\partial a_i \partial a_j}, \quad i,j = 1,...,6. \tag{11}$$

The condition for $C_{22}-C_{23}=0$, with the aid of Eq. (9), becomes

$$\frac{\partial^2 E}{\partial a_2^2} - \frac{\partial^2 E}{\partial a_2 \partial a_3} = \frac{F' a_2^2}{4} \sum (l_2^4 - l_2^2 l_3^2) f'' + \frac{a_2^2}{8} \sum (l_2^4 - l_2^2 l_3^2) \phi'' + \frac{F'}{2} \sum l_2^2 f' + \frac{1}{4} \sum l_2^2 \phi' = 0. \tag{12}$$

Also, if the crystal is under uniaxial load coaxial with $\mathbf{a}_1$, $F'\Sigma l_2^2 f' + \frac{1}{2}\Sigma l_2^2 \phi'$ vanishes, as seen from Eqs. (6) or (7) and (10). Thus, in the EAM, the condition for the $C_{22}=C_{23}$ eigenstate reduces to

$$F' \sum (l_2^4 - l_2^2 l_3^2) f'' + \tfrac{1}{2} \sum (l_2^4 - l_2^2 l_3^2) \phi'' = 0. \tag{13}$$

III. RESULTS AND DISCUSSION

Figures 1–5 show the mechanical responses, in the range of axial stretch $0.9 \leqslant \lambda_a \leqslant 1.1$, of four representative metals that comprise a ''standard'' fcc metal (Cu), a ''standard'' bcc metal (Na), an ''anomalous'' fcc metal (Al), and a bcc group-VI transition metal (Mo). The response of Na, originally in its fcc configuration, is also included since, at low temperatures, Na exists in a close-packed phase, equivalent to fcc with stacking faults; additionally, it is instructive to compare the responses of a bcc and an fcc crystal described with the identical EAM model. The initial slopes (i.e., at $\lambda_a=1$) of the σ_a (axial stress) versus λ_a (axial stretch) curves are the initial Young moduli and the initial slopes of the λ_t (transverse stretch) versus λ_a curves are the (negative) Poisson ratios at zero stress. The moduli of course vary with strain.

Figure 1 shows the behavior of Cu, in which the initial ordering of the Young moduli is seen to be $E_{111} > E_{110} > E_{100}$ and the initial Poisson's ratios are ordered according to $\nu_{110}^{001} > \nu_{100} > \nu_{111} > 0 > \nu_{110}^{\bar{1}10}$. The upward concavity of the initial [100] σ_a vs λ_a curve is also evident; this concavity is naturally associated with the well-known Bain transformation, which has been widely viewed as a mechanism for fcc↔bcc transitions under tetragonal lattice distortions.[27,28] A related phenomenon is the relatively shallow minimum stress σ_a on the [100] path in compression. Under high compression, the [110] loading path becomes ''stiffest,'' as expected, since [110] is the direction of closest approach of neighboring atoms in an fcc structure. In the range of behavior depicted in Fig. 1, under [110] loading the transverse stretch in the [110] direction is always positive under tension

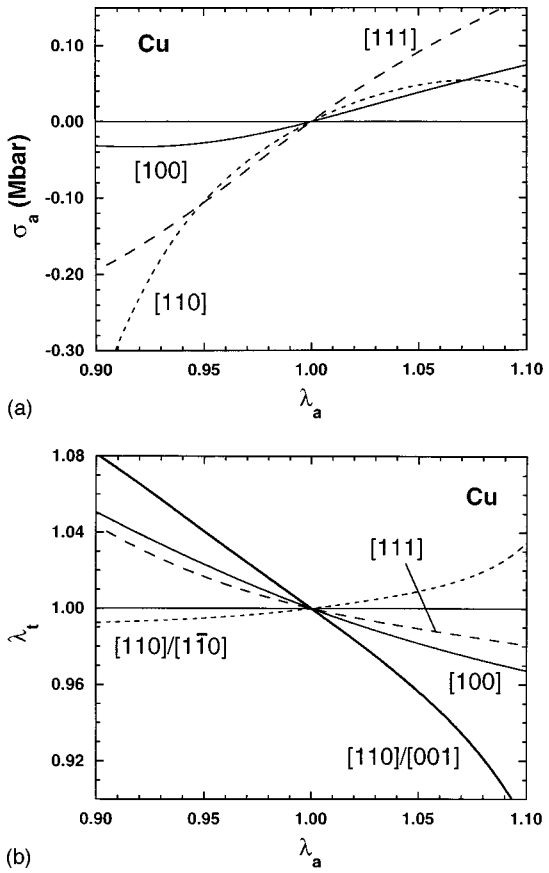

FIG. 1. Mechanical response of face-centered-cubic copper. (a) Uniaxial stresses σ_a applied along the [100], [110], and [111] directions vs axial stretch λ_a (1 Mbar=100 GPa), and (b) stretches λ_t transverse to the loading directions [100], [111], and [110] vs axial stretch λ_a; the transverse stretches under [100] and [111] loading are isotropic; under [110] loading, the transverse stretches λ_t^{001} along the [001] direction and λ_t^{110} along the [$\bar{1}$10] direction are designated by the nomenclature [110]/[001] and [110]/[110], respectively.

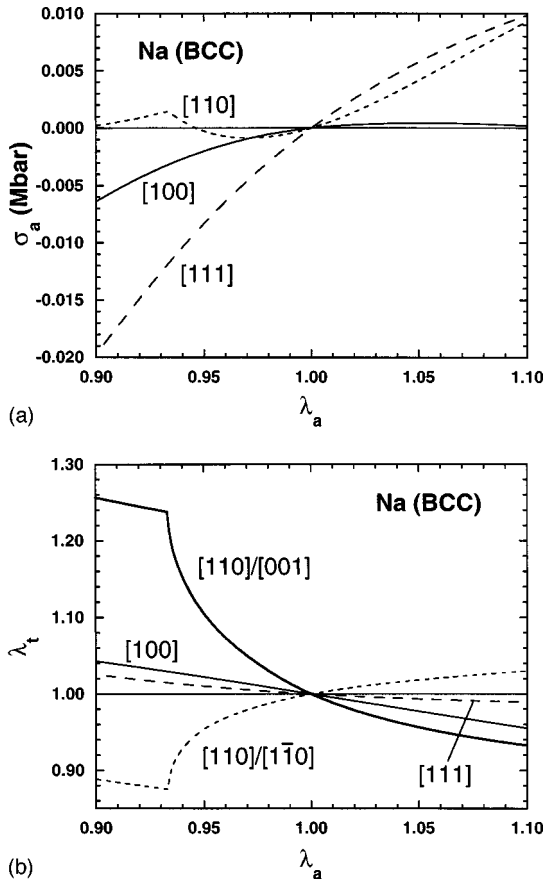

FIG. 2. Mechanical response of body-centered-cubic sodium. See descriptions of (a) and (b) in Fig. 1 for descriptions of (a) and (b) in this figure.

and negative under compression; the [001] transverse stretch is of opposite sign, and the variation of its magnitude is greater than that of any of the other transverse stretches. In the region of high λ_a, the rate of changes of the magnitudes of the transverse stretches under [110] loading increase markedly with increasing λ_a; in fact, as the state is approached where the [110] path branches from the [100] path, $d\lambda_t^{001}/d\lambda_a \to -\infty$ and $d\lambda_t^{110}/d\lambda_a \to \infty$; for the EAM model of Cu, this state occurs in a region of compressive loading at the point where $C_{44}=0$, relative to the axes of the face-centered-tetragonal computational cell (or equivalently, where $C_{22}=C_{23}$, relative to the body-centered-tetragonal axes), on the [100] path. The existence of this bifurcation also causes the maximum stress $\sigma_{a\text{-max}}$ on the [110] path to be relatively depressed, as the [110] tensile loading curve ''bends over'' to meet the [100] loading curve at the branch point. The actual bifurcation occurs at $\lambda_a=1.124$ on the [110] path, out of the range depicted in Fig. 1; however, its presence clearly influences the mechanical response throughout the full [110] path. A distinct (but analogous) bifurcation occurs at $\lambda_a=1.133$ on the [100] path of Cu, at a tensile stress of 9.8 GPa, at the state where $C_{22}=C_{23}$ relative to the axes of the face-centered-tetragonal cell; the occurrence of this state provides an upper bound to the theoretical strength of Cu in [100] uniaxial loading[29] (1 Mbar=100 GPa). The stress at which this occurs is less than half the maximum [100] tensile stress (of 23.7 GPa at $\lambda_a=1.381$).

The behaviors of bcc and fcc Na are shown in Figs. 2 and 3, respectively. For both structures, the respective orderings of the initial Young's moduli and Poisson's ratios are seen to be $E_{111}>E_{110}>E_{100}$ and $\nu_{110}^{001}>\nu_{100}>\nu_{111}>0>\nu_{110}^{\bar{1}10}$. Under increasing compression, the [111] path of the bcc structure continues to be the stiffest; this agrees with intuition, since [111] is the direction of closest approach for atoms in a bcc crystal. The extremely small value of maximum tensile stress $\sigma_{a\text{-max}}$ on the [100] path of the bcc structure [Fig. 2(a)] is owing to the aforementioned Bain transformation, as is the small compressive stress on the [100] path of the fcc structure [Fig. 3(a)]. (The body-centered-tetragonal and face-centered-tetragonal structures are identical at a given value of a_1 under uniaxial load, so the [100] paths shown in Figs. 2 and 3 just comprise different sections of the same path, but with separate reference states at $\lambda_a=1$.) In each of the loading directions, the behavior of fcc Na is qualitatively similar to that of fcc Cu, except that, for fcc Na, the bifurcation, under which the [110] path branches from the [100] path, occurs within the range depicted in the figures. This is evident in Figs. 3(a) and 3(b) at an axial stretch of 1.081 on the [110] path of the initially fcc structure, where the slopes of the σ_a and λ_t curves change abruptly; for values of λ_a

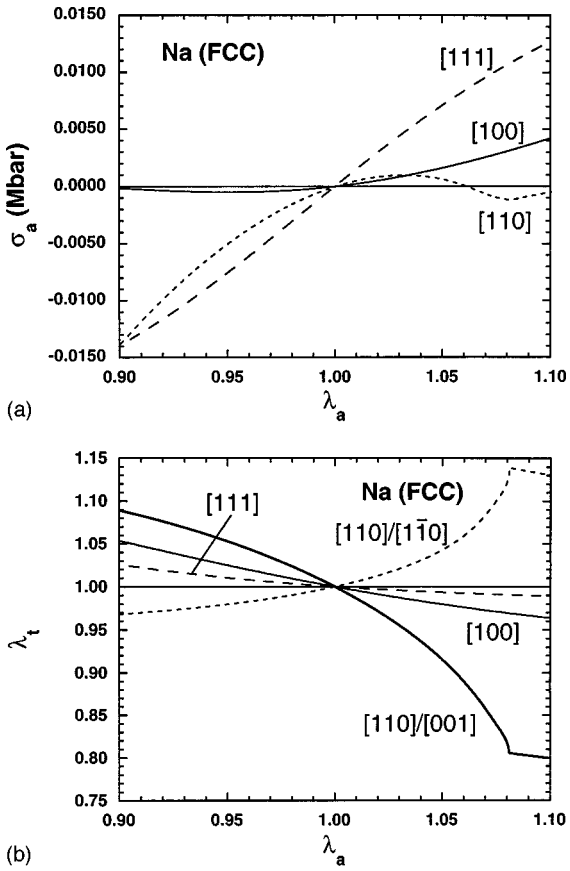

FIG. 3. Mechanical response of face-centered-cubic sodium. See descriptions of (a) and (b) in Fig. 1 for descriptions of (a) and (b) in this figure.

>1.081 on this path, the structure is tetragonal, rather than orthorhombic, and thus this section of the [110] path also resides on the [100] path. An analogous bifurcation is seen in Figs. 2(a) and 2(b) on the [110] path of initially bcc Na at an axial stretch of 0.933; for $\lambda_a < 0.933$, the structure is likewise tetragonal, rather than orthorhombic, so this portion of the [110] path is thus also equivalent to [100] loading. This bifurcation occurs in a region of tensile loading on the [100] path of bcc Na at the point where $C_{44}=0$, relative to the axes of the body-centered-tetragonal computational cell, or equivalently, where $C_{22}=C_{23}$, relative to the face-centered-tetragonal axes (i.e., to the axes of the computational cell under [100] loading of the fcc structure). The existence of this bifurcation, wherein the load on the [110] path has ''turned upward'' to meet the [100] path in a region of tensile loading (or equivalently, where the load on the [110] path has dropped suddenly from the [100] path), may be considered responsible for the upward concavity of the [110] stress-strain relation of the bcc structure and for the relatively small maximum compressive stress on this path. (The ''meeting'' of these curves is not apparent in the figures depicted here, since the initial states (i.e., at $\lambda_a=1$) on the diverse paths are reckoned to different crystal axes. In order to view directly the convergence of the [100] and [110] loading paths at a single point, where $C_{22}=C_{23}$, the values of stretch on both the [110] and [100] paths would need to be reckoned to the same set of crystal axes.)

The behavior of the EAM model of Al is shown in Fig. 4.

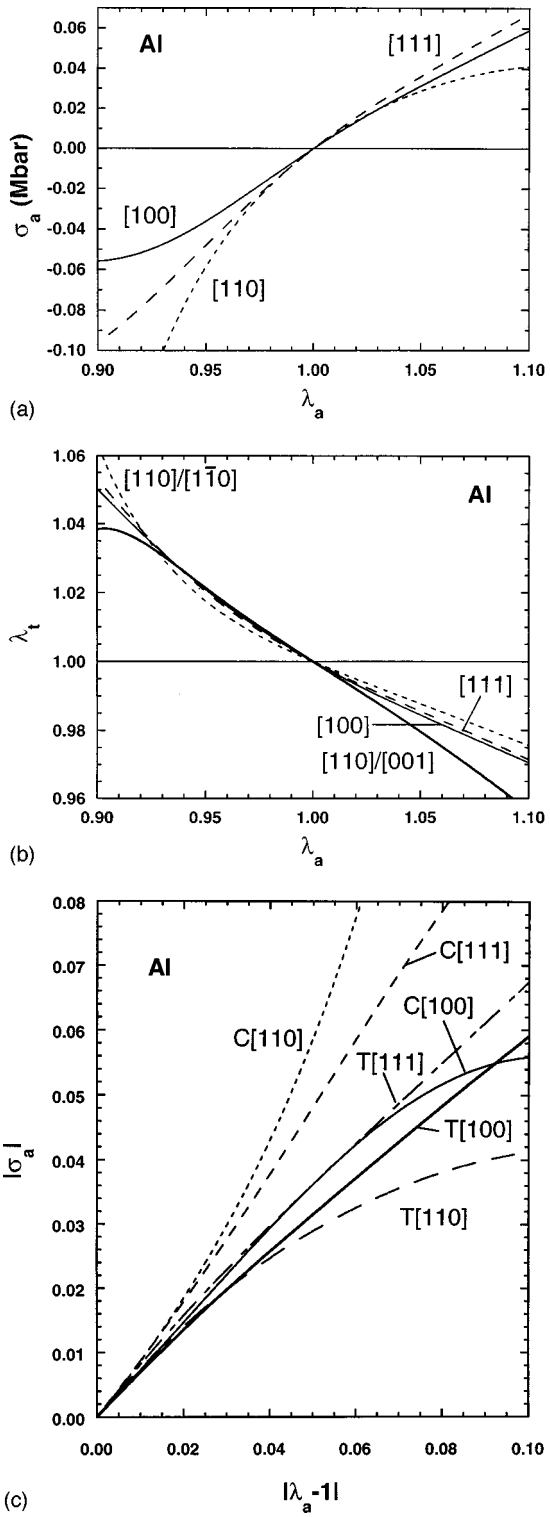

FIG. 4. Mechanical response of face centered cubic aluminum. See descriptions of (a) and (b) in Fig. 1 for descriptions of (a) and (b) in this figure. (c) Absolute values of uniaxial stress $|\sigma_a|$ (Mbar) in compression C and in tension T vs absolute value of strain $|\lambda_a - 1|$.

Aluminum is characterized by a lack of strong anisotropy that extends over relatively large ranges of uniaxial loading. The initial Poisson ratios are all positive, and remain so over large ranges of λ_a; the axial stress is initially concave downward under [100] loading, but becomes concave upward un-

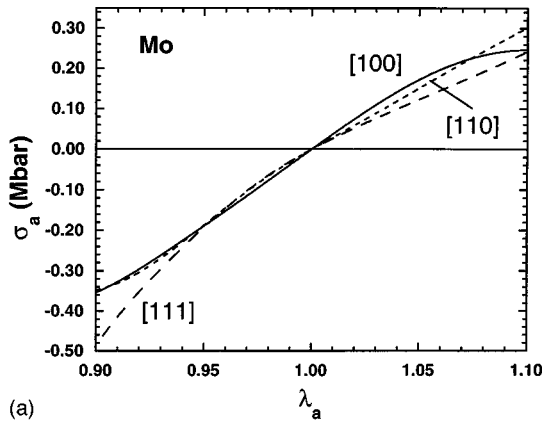

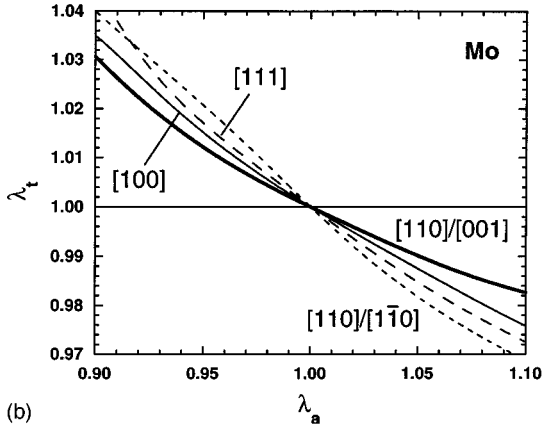

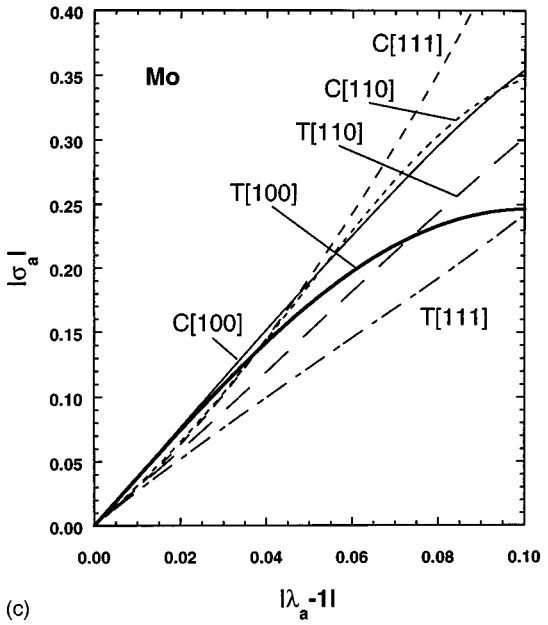

FIG. 5. Mechanical response of body-centered-cubic molybdenum. See descriptions of (a) and (b) in Fig. 1 for descriptions of (a) and (b) in this figure and see description of (c) in Fig. 4 for description of (c) in this figure.

der [100] compressive loading, owing to the influence of the Bain transformation. While the initial slopes of the σ_a vs λ_a curves are similar, the [110] path exhibits considerable curvature and diverges most rapidly, in both compression and tension, from the initial grouping of stress-strain curves, as is seen in Fig. 4(c). Although the EAM model of Al exhibits a bifurcation of the type experienced on the [110] paths of the fcc models of Cu and Na, the bifurcation occurs at a relatively large value of λ_a on aluminum's [110] path, i.e., at $\lambda_a = 1.233$, and thus does not have as strong an influence on the [110] loading behavior as is observed for fcc Na and Cu. Under increased tensile loading, however, the axial stress on the [110] path does achieve a lower maximum stress than on either the [100] or the [111] paths, owing to the incipient bifurcation. In other words, Al is qualitatively similar to the other fcc metals in that the theoretical maximum tensile stress on the [110] path is strongly influenced by critical crystal symmetries, and is not the stress inherent in the strength of the atomic bonds.

Figure 5 shows the mechanical response of bcc Mo, which may be contrasted with that of bcc Na in Fig. 2. Although the anisotropy of Mo is not as great as that of the bcc alkali metals, or of the fcc metals (excluding Al), the ''reverse'' orderings $E_{100} > E_{110} > E_{111}$ and $\nu_{110}^{110} > \nu_{111} > \nu_{100} > \nu_{110}^{001} > 0$ are clearly evident in Figs. 5(a) and 5(b), respectively. Although [111] is the ''softest'' direction initially, it becomes stiffest under increased compressive loading, as might be expected. The [100] tensile path also exhibits a relatively low maximum stress, although the ratios of the maximum tensile stresses on the [100], [110], and [111] paths, respectively, are 1:2.4:2.8 in Mo, compared with 1:47:34 for these ratios in bcc Na. In part, the much smaller anisotropy of the maximum stresses in Mo, when compared with Na, is understood from the relative anisotropies of the initial Young's moduli E_{hkl}. However, this contrast persists, in particular when [110] is compared with [100] and [111] loadings, even when the differences in the E_{hkl} are ''factored out.'' That is, if $\sigma_{a\text{-max}}/E$ represents the maximum tensile stress in the $[hkl]$ direction divided by the initial slope E_{hkl} of the stress-strain curve, then the ratios of $\sigma_{a\text{-max}}/E$ in the [100], [110], and [111] directions, respectively, are 1:3.1:3.8 in Mo and 1:17:4.9 in bcc Na. The relatively large maximum tensile stress in [110] loading of bcc Na apparently is owing to the upward concavity of the [110] stress-strain curve, which remains concave upward over a very large region of tensile and compressive loading and which, in turn, is owing to the bifurcation seen in Fig. 2 and discussed earlier. Although the [110] path of the bcc structure of Mo also branches from the [100] path, as in the case of bcc Na (and of the other bcc metals), for Mo this path branches with a positive slope of σ_a vs λ_a at the point of bifurcation. This type of response has not been reported in the literature previously. We plan, in due course, to provide a detailed exposition of the characteristic modes of bifurcation, including the roles of the elastic moduli (up to, and including, the fourth-order moduli C_{ijkl} at the branch point[24]). While the branching behavior of Mo is complex (e.g., under very high compression, the orthorhombic [110] σ_a vs λ_a uniaxial loading path ceases to be a simple, single-valued function), the bifurcation occurs in a region where it does not influence the [110] loading path significantly within the range depicted in Fig. 5. While the *relative* ''accessibility'' of the branch points on the [110] and [100] paths of Na apparently is associated with the ''ease'' of phase transitions in that metal,[5,6] the relative ''inaccessibility'' of these states in Mo is con-

TABLE I. Initial values of Young's moduli E, theoretical ultimate tensile stresses $\sigma_{a\text{-max}}$, and theoretical ultimate tensile loads per unit reference area $L_{a\text{-max}}$ for the bcc metals under [100], [110], and [111] uniaxial loading and theoretical stress $\sigma_{a\text{-crit}}$ for these metals at the $C_{22}=C_{23}$ eigenstate in [100] loading.

Mechanical property (Mbar)	Mode of loading	Metals						
		Nb	Mo	Fe	Rb	K	Na	Li
E	[100]	1.530	3.814	1.189	7.55×10^{-3}	0.0109	0.0201	0.0335
E	[110]	0.916	3.024	2.104	0.0193	0.0294	0.0558	0.0961
E	[111]	0.808	2.829	2.831	0.0399	0.0681	0.137	0.255
$\sigma_{a\text{-max}}$	[100]	0.140	0.247	0.0599	2.05×10^{-4}	3.20×10^{-4}	4.19×10^{-4}	2.75×10^{-4}
$\sigma_{a\text{-max}}$	[110]	0.215	0.603	0.331	6.14×10^{-3}	9.75×10^{-3}	0.0195	0.0291
$\sigma_{a\text{-max}}$	[111]	0.419	0.696	0.300	4.40×10^{-3}	7.06×10^{-3}	0.0142	0.0273
$L_{a\text{-max}}$	[100]	0.107	0.235	0.0553	1.94×10^{-4}	3.01×10^{-4}	3.99×10^{-4}	2.71×10^{-4}
$L_{a\text{-max}}$	[110]	0.194	0.557	0.306	5.77×10^{-3}	9.33×10^{-3}	0.0186	0.0283
$L_{a\text{-max}}$	[111]	0.349	0.615	0.264	3.78×10^{-3}	6.36×10^{-3}	0.0126	0.0250
$\sigma_{a\text{-crit}}$	[100]	2.526	−0.885	−0.143	-6.08×10^{-3}	-8.89×10^{-3}	-1.19×10^{-3}	-9.03×10^{-3}

cordant with the high degree of stability of the bcc structure of this metal.

Numerical values indicative of the theoretical mechanical responses of the bcc metals Nb, Mo, Fe, Rb, K, Na, and Li and of the fcc metals Al, Ni, Cu, Ag, Au, and Na are listed in Tables I–V. It is interesting to note that bulk structural materials, such as steels, can achieve tensile strengths (i.e., true stresses at failure) of over 2 GPa (see, e.g., Kelly,[30] pp. 138–148) and Fe whiskers in [111] loading have reached breaking strengths of 13 GPa, as discussed by Kelly,[30] pp. 36–39, based on the work of Brenner.[31] Tables I and II indicate that the theoretical maximum tensile stresses, $\sigma_{a\text{-max}}$, for bcc transition metals Nb, Mo, and Fe are in the range of about 6 GPa (for Fe in [100] loading) to 70 GPa (for Mo in [111] loading) and, for the fcc structural metals Al, Ni, and Cu, in the range of about 4.2 GPa (for Al in [110] loading) to 39 GPa for Ni in [100] and [111] loading. The theoretical maximum stresses are greater than the actual ultimate tensile strengths, as would be expected; however, the theoretical values are generally within about an order of magnitude of the upper range of experimental values. Also, Kelly[30] reports the breaking strengths of Cu and Ag whiskers tested by Brenner; the strongest directions were [111] and [100]; the best Cu and Ag whiskers broke at 2.94 and 1.73 GPa, respectively; i.e., Cu was 1.7 times stronger than Ag. From Table II, we note that the theoretical maximum loads per unit reference area, $L_{a\text{-max}}$, are 1.7 times greater for Cu than for Ag in [100] loading and 1.9 times greater in [111] loading. In [100] loading, the theoretical strength is reduced by the onset of instability when $C_{22}=C_{23}$, which occurs at 3.8 GPa for Ag and 9.8 GPa for Cu. The EAM models of Cu and Ag thus appropriately reflect the relative strengths of these metals, when compared with experimental values of whisker strengths.

For a given metal and a given loading direction, the maximum stress and the maximum load occur within proximity of each other, as seen in Table III. For the group-V and group-VI transition metals (i.e., Nb and Mo), the loading direction with the greatest values of maximum stress $\sigma_{a\text{-max}}$ is [111] and the direction with the smallest $\sigma_{a\text{-max}}$ values is [100], as seen in Table I; the ratio of $\sigma_{a\text{-max}}$ in the [111] direction to $\sigma_{a\text{-max}}$ in [100] is about 3 for both of these metals; this behavior is relatively isotropic. For Fe and the bcc alkali metals, the greatest value of $\sigma_{a\text{-max}}$ occurs in [110]

TABLE II. Initial values of Young's moduli E, theoretical ultimate tensile stresses $\sigma_{a\text{-max}}$, and theoretical ultimate tensile loads per unit reference area $L_{a\text{-max}}$ for the fcc metals under [100], [110], and [111] uniaxial loading and theoretical stress $\sigma_{a\text{-crit}}$ for these metals at the $C_{22}=C_{23}$ eigenstate in [100] loading.

Mechanical property (Mbar)	Mode of loading	Metals					
		Al	Ni	Cu	Ag	Au	Na
E	[100]	0.708	1.385	0.725	0.449	0.425	0.0209
E	[110]	0.801	2.335	1.410	0.841	0.807	0.0592
E	[111]	0.837	3.026	2.058	1.185	1.153	0.152
$\sigma_{a\text{-max}}$	[100]	0.126	0.390	0.237	0.127	0.225	0.0210
$\sigma_{a\text{-max}}$	[110]	0.0418	0.117	0.0547	0.0202	0.0284	9.73×10^{-4}
$\sigma_{a\text{-max}}$	[111]	0.148	0.393	0.265	0.136	0.214	0.0196
$L_{a\text{-max}}$	[100]	0.103	0.327	0.201	0.116	0.188	0.0180
$L_{a\text{-max}}$	[110]	0.0386	0.110	0.0517	0.0192	0.0261	9.47×10^{-4}
$L_{a\text{-max}}$	[111]	0.125	0.370	0.245	0.129	0.197	0.0191
$\sigma_{a\text{-crit}}$	[100]	0.111	0.213	0.0982	0.0382	0.100	1.46×10^{-3}

TABLE III. Values of axial stretch λ_a at states of maximum tensile stress $\sigma_{a\text{-max}}$ and at states of maximum tensile load (per unit reference area) $L_{a\text{-max}}$ under [100], [110], and [111] uniaxial loading and at the critical $C_{22}=C_{23}$ eigenstate in [100] loading. (Example: in Nb, $\sigma_{a\text{-max}}$ and $L_{a\text{-max}}$ occur at $\lambda_a=1.104$ and 1.102, respectively, under [100] loading and at $\lambda_a=1.153$ and 1.152, respectively, under [111] loading.)

Metal	Initial structure	λ_a under [100] loading	λ_a under [110] loading	λ_a under [111] loading	λ_a at $C_{22}=C_{23}$ in [100] loading
Nb	bcc	1.104, 1.102	1.153, 1.152	1.290, 1.283	0.747
Mo	bcc	1.101, 1.099	1.246, 1.246	1.276, 1.270	0.756
Fe	bcc	1.107, 1.101	1.262, 1.263	1.244, 1.225	0.904
Rb	bcc	1.062, 1.060	1.323, 1.329	1.278, 1.249	0.953
K	bcc	1.067, 1.065	1.311, 1.319	1.234, 1.213	0.953
Na	bcc	1.053, 1.051	1.297, 1.300	1.250, 1.225	0.964
Li	bcc	1.017, 1.017	1.332, 1.323	1.200, 1.192	0.983
Al	fcc	1.386, 1.348	1.113, 1.108	1.302, 1.290	1.233
Ni	fcc	1.362, 1.357	1.086, 1.084	1.219, 1.220	1.183
Cu	fcc	1.381, 1.371	1.074, 1.072	1.245, 1.239	1.133
Ag	fcc	1.273, 1.173	1.060, 1.057	1.206, 1.205	1.060
Au	fcc	1.207, 1.201	1.100, 1.097	1.178, 1.177	1.102
Na	fcc	1.449, 1.450	1.032, 1.031	1.244, 1.248	1.046

loading and the least in [100] loading; the ratio of the ''greatest'' to the ''least'' is 5.5 for Fe and it varies from about 30 to 100 for the bcc alkali metals, which are thus highly anisotropic in this regard. The behavior of Fe is ''intermediate,'' when compared with the bcc alkalis and the bcc group-V and group-VI transition metals. For a given fcc metal, under [100] and [111] loading, the theoretical values of $\sigma_{a\text{-max}}$ are generally comparable, and are from about 3 to 20 times larger than $\sigma_{a\text{-max}}$ under [110] loading, as is seen from Table II. In Table III it is observed that the maximum tensile stresses in Nb, Mo, and Fe occur at axial strains of about 10% in [100] loading, 25% in [110] loading (except for Nb), and 25–30% in [111] loading. For the bcc alkali metals, these axial strains are, respectively, about 2–7%, 30%, and 20–30%. For each of the bcc metals, except Nb, both the maximum stresses (Table I) and the corresponding stretches (Table III) are comparable in the [110] and [111] directions. Nb is unusual, in that the [110] *tensile* path contains an unstressed face-centered-orthorhombic configuration. For the fcc metals other than Na, the maximum stresses and loads occur at axial strains of about 20–40% in [100] loading, 5–10% in [110] loading, and 20–30% in [111] loading; among these fcc metals, Al exhibits the greatest strain at $\sigma_{a\text{-max}}$ for each direction of loading. Face-centered-cubic Na exhibits a particularly large difference between the strains at $\sigma_{a\text{-max}}$ in the [100] and [110] directions.

For the bcc metals in [100] loading, the $C_{22}=C_{23}$ eigenstates occur under compressive stretches of about 0.75 in Nb

TABLE IV. Normalized maximum tensile stresses $\sigma_{a\text{-max}}/E$ for crystals under uniaxial load coincident with the [100], [110], and [111] directions; normalized axial stress $\sigma_{a\text{-crit}}/E$ at the $C_{22}=C_{23}$ eigenstate in [100] loading; and $\sigma_{a\text{-crit}}/\sigma_{a\text{-max}}$ in [100] loading. The initial Young modulus (or initial slope of the stress-strain curve) under the respective mode of loading is E.

Metal	Initial structure	$\sigma_{a\text{-max}}/E$ in [100]	$\sigma_{a\text{-max}}/E$ in [110]	$\sigma_{a\text{-max}}/E$ in [111]	$\sigma_{a\text{-crit}}/E$ in [100]	$\sigma_{a\text{-crit}}/\sigma_{a\text{-max}}$ in [100]
Nb	bcc	0.0746	0.235	0.519	1.652	22.151
Mo	bcc	0.0647	0.199	0.246	−0.232	−3.587
Fe	bcc	0.0504	0.157	0.106	−0.120	−2.384
Rb	bcc	0.0272	0.319	0.110	−0.0805	−2.959
K	bcc	0.0294	0.331	0.104	−0.0817	−2.781
Na	bcc	0.0209	0.350	0.103	−0.0595	−2.852
Li	bcc	8.21×10^{-3}	0.303	0.107	−0.0269	−3.279
Al	fcc	0.178	0.0522	0.176	0.157	0.879
Ni	fcc	0.281	0.0503	0.130	0.154	0.547
Cu	fcc	0.327	0.0388	0.129	0.135	0.414
Ag	fcc	0.283	0.0240	0.114	0.0850	0.301
Au	fcc	0.529	0.0352	0.186	0.236	0.445
Na	fcc	1.004	0.0164	0.129	0.0696	0.0693

TABLE V. Values of transverse stretch λ_t at states of maximum tensile stress $\sigma_{a\text{-max}}$ under [100], [110], and [111] uniaxial loading and at the $C_{22}=C_{23}$ eigenstate in [100] loading. The transverse stretch is isotropic under [100] and [111] loading. Under [110] loading, two values of transverse stretch are indicated; these are reckoned, respectively, along the orthogonal directions [110] and [001] (relative to the initial cubic structure); these directions are of course also orthogonal to the [110] loading direction.

Metal	Initial structure	λ_t under [100] loading	λ_t under [110] loading	λ_t under [111] loading	λ_t at $C_{22}=C_{23}$ in [100] loading
Nb	bcc	0.967	0.914, 0.986	0.911	1.104
Mo	bcc	0.976	0.979, 0.944	0.940	1.104
Fe	bcc	0.960	1.039, 0.888	0.935	1.036
Rb	bcc	0.972	1.052, 0.894	0.922	1.021
K	bcc	0.970	1.069, 0.895	0.946	1.021
Na	bcc	0.976	1.059, 0.898	0.939	1.016
Li	bcc	0.992	1.092, 0.891	0.955	1.008
Al	fcc	0.902	0.972, 0.950	0.918	0.933
Ni	fcc	0.915	1.009, 0.930	0.971	0.946
Cu	fcc	0.920	1.071, 0.929	0.960	0.959
Ag	fcc	0.954	1.008, 0.947	0.975	0.979
Au	fcc	0.914	0.997, 0.922	0.960	0.958
Na	fcc	0.924	1.022, 0.952	0.987	0.981

and Mo, 0.9 in Fe, and 0.95–0.98 in the bcc alkali metals; here, again, the behavior of Fe is ''intermediate.'' For the fcc metals, these states occur under tensile stretches ranging from about 1.05 for Na to 1.23 for Al. Since the $C_{22}=C_{23}$ eigenstates can limit the theoretical tensile strengths of fcc crystals in [100] loading, it is of particular interest to examine where these states occur relative to the states of maximum stress $\sigma_{a\text{-max}}$ on the [100] paths. Among the fcc crystals, the ''critical stress'' $\sigma_{a\text{-crit}}$, at which $C_{22}=C_{23}$, varies from about 90% of $\sigma_{a\text{-max}}$, for Al, to about 7% of $\sigma_{a\text{-max}}$, for Na. For most of the fcc metals included in the present study, $\sigma_{a\text{-crit}}/\sigma_{a\text{-max}}$ is in the approximate range of 0.3–0.5. The corresponding strains at $\sigma_{a\text{-crit}}$ range from about 10% (for Na) to 60% (for Al) of the strains at $\sigma_{a\text{-max}}$.

In order to gain a firmer understanding of the role of ''structure,'' as distinct from ''bond strength,'' it is useful to examine the normalized stress-strain responses of each metal, i.e., wherein the axial stress σ_a is divided by the initial Young's modulus E appropriate to the particular metal and specific loading direction. Table IV shows the normalized maximum tensile stresses under [100], [110], and [111] loading and the critical stresses at $C_{22}=C_{23}$ in [100] loading and Figs. 6(a)–6(c) show the normalized, tensile, stress-strain curves of the bcc metals Na and Mo and the fcc metals Na, Cu, and Al over ranges of axial stretch that include the maximum theoretical tensile stresses $\sigma_{a\text{-max}}$. The influence of crystal symmetry is clearly evident in Figs. 6(a) and 6(b); the maximum values σ_a/E under uniaxial tensile loading are relatively small and occur at relatively small values of λ_a for the bcc metals in [100] loading and in the fcc metals in [110] loading. The striking differences between the theoretical responses of bcc and fcc crystals observed in Figs. 6(a) and 6(b) are absent in Fig. 6(c). For example, for Na, the values of $\sigma_{a\text{-max}}/E$ of the bcc and fcc crystals under [111] tensile loading are within about 25% of each other, whereas these values differ by factors of about 50 under [100] loading and 20 under [110] loading. The theoretical tensile [111] loading paths of bcc crystals pass through the unstressed simple cubic (sc) states when the ratio of axial to transverse stretch, λ_a/λ_t, is doubled.[32] However, since these sc states tend to reside at significantly greater energies than either the bcc or fcc unstressed configurations, the ''stress barriers'' for transforming the crystals from the bcc to the sc states under [111] loading (i.e., the maximum [111] tensile stresses for bcc crystals) are generally quite large. In fact, these stress barriers are close to the theoretical maximum stresses $\sigma_{a\text{-max}}$ in [110] tensile loading of bcc crystals; these values, in turn, are indicative of the inherent strength of the atomic bonds, i.e., they are limited neither by crystallographic transformations among unstressed states (e.g., the Bain transformation) nor bifurcation phenomena (with the exception of Nb, as is mentioned above).

The characteristic responses of the crystals to homogeneous, finite, strain may also affect inhomogeneous behavior critically. For example, Abraham[26] has modeled crack propagation under very rapid [100], [110], and [111], uniaxial, tensile, loading of an fcc crystal with Lennard-Jones interatomic interactions; the cracks were oriented in such a manner that the plane in which the propagation occurred was perpendicular to the direction of load. He found the crack to propagate in a brittle manner under [110] loading, whereas under [100] and [111] loading, crack propagation was blunted by the emission of dislocations at the crack tip. Abraham attributed the brittle mode of crack propagation under [110] loading to the relatively low theoretical maximum tensile strength of the perfect crystal under [110] loading. Here we demonstrate the generality of this ''depressed'' stress-strain response to [110] tensile loading of fcc crystals, and emphasize the influence of the bifurcation process on the loading response. The present work also demonstrates the generality of the relatively low theoretical tensile strength of bcc crystals under [100] loading, and suggests that, in simu-

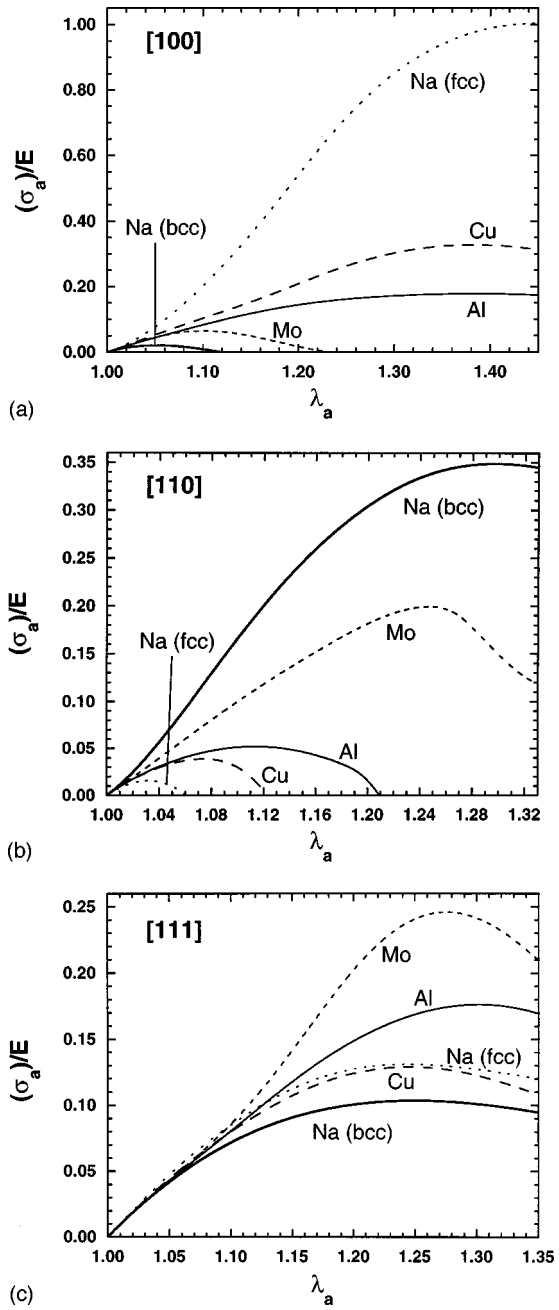

FIG. 6. Mechanical response of the fcc metals Na, Cu, and Al and the bcc metals Na and Mo to unconstrained uniaxial tensile loading in the three principal symmetry directions; σ_a/E represents the uniaxial stress applied to the crystal in the $[hkl]$ direction divided by the initial slope of the stress-strain (or stress-stretch) curve (i.e., divided by the initial Young's modulus, E_{hkl}) and λ_a is the stretch coaxial with the load. The numerical values of E for each metal, for each loading axis, are given in Tables I and II. The crystals are loaded in (a) the [100] (or ''cube-edge'') direction, (b) the [110] (or ''face-diagonal'') direction, and (c) the [111] (or ''body-diagonal'') direction.

lations such as those performed by Abraham, crack propagation under [100] loading of bcc crystals may be similar to that of fcc crystals under [110] loading.

Abraham also found that, under [100] loading of the fcc Lennard-Jones crystal, dislocations were emitted from the crack tip in an ordered geometrical pattern, whereas under [111] loading, dislocations were generated in a more random, disordered manner. One may speculate that the differences are owing to the $C_{22}=C_{23}$ eigenstate, which always has been found to occur in the tensile region of the [100] path of fcc crystals, before the maximum stress $\sigma_{a\text{-max}}$ is reached. It is likely that the incipient crystal bifurcation associated with this eigenstate is responsible for the ''order'' under which the dislocations are emitted. The generality of the occurrence of this eigenstate also imparts generality to the behavior of Abraham's fcc Lennard-Jones crystal under [100] loading. Since an analogous state has not been found on the *tensile* paths of the bcc crystals, one further may speculate that such ordered emission of dislocations would be unlikely during rapid loading of bcc crystals in such simulations.

In earlier work[11,12,32–36] Milstein and co-workers studied the uniaxial loading behavior of crystals using Morse[33] and generalized Morse[35] potentials to model interatomic bonding. Such purely central-force models are known to posses Cauchy symmetries among the elastic moduli, e.g., $C_{44}=C_{23}$, $C_{55}=C_{13}$, and $C_{66}=C_{12}$ for body-centered-orthorhombic or face-centered-orthorhombic crystals, which reduces to $C_{12}=C_{44}$ for cubic crystals. Thus, in the central force approximation, it may be possible to model accurately the experimental values of C_{11} and C_{12} or of C_{11} and C_{44} of cubic metals, but not of C_{11}, C_{12}, and C_{44}, except in fortuitous cases where, experimentally, $C_{12}\approx C_{44}$, which is not a common occurrence. Additional restrictions are of course placed on the third-order moduli of central-force crystals; thus it is clear that such models are limited in their ability to reproduce *quantitatively* the complete harmonic and anharmonic, anisotropic, elastic response of metal crystals. Milstein chose to fit the three Morse parameters to experimental values of the unstressed atomic volume and elastic moduli C_{11} and C_{12}; this ensured that the initial slope [i.e., $C_{11}-2C_{12}^2/(C_{11}+C_{12})$] of the [100] loading path agreed with experiment. (The fcc crystals accommodated such fittings, but bcc crystals could not be modeled in this manner, with the exception of alkali metals.) Despite these deficiencies, the fcc crystals and the bcc alkali metals modeled in this manner exhibited behavior, including bifurcation phenomena, that is qualitatively similar to that found in the present study. For example, Milstein and Rasky[12] used such a Morse model to study the loading behavior of fcc Cu; Fig. 7 shows their results, with comparisons to the loading behavior of Cu in the present study. The present computations are of course considered more reliable, since EAM models rest upon a firmer theoretical foundation[8] than purely central-force models of metals, and the present EAM model reproduces all three second-order and all six third-order elastic moduli. Nevertheless, the qualitative agreement between the Morse and EAM loading behaviors is remarkable. This comparison further emphasizes the roles of crystalline symmetries and the general nature of interatomic forces as controlling influences on the mechanical responses of the fcc metals; similar comparisons can be made for the bcc alkali metals. The group-V and group-VI bcc transition metals, however, behave uniquely, both in their infinitesimal loading response and in their ''bifurcation activity'' under large strain. In order to model these responses, it has been necessary to em-

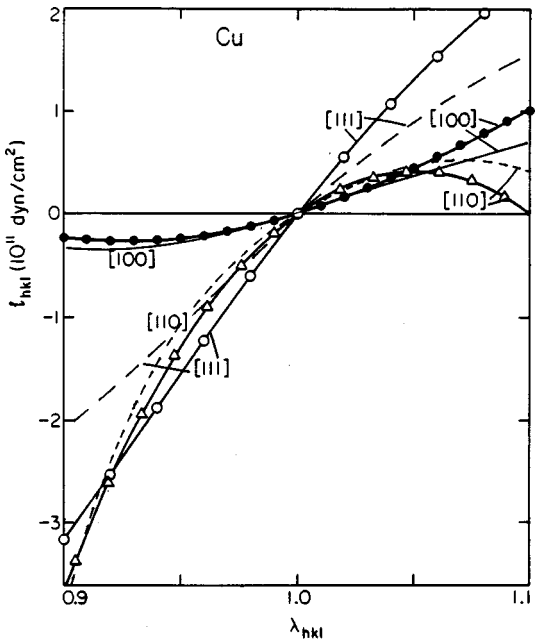

FIG. 7. Mechanical response of the Morse potential model of Cu (reproduced from Ref. 12) and the EAM model (present work); the solid lines containing ''data points'' are from Ref. 12. The symbols l_{hkl} and λ_{hkl} are equivalent to L_a and λ_a in the present study.

ploy models that are more sophisticated than those that rely only on the general nature of interatomic forces, such as the Morse interactions.

IV. SUMMARY AND CONCLUSIONS

This is the first of several papers that explore the theoretical elastic behavior of metals at finite strain in the framework of the embedded-atom method. As a means to this end, EAM models that incorporate empirical values of both the second- and the third-order elastic moduli have been constructed for twelve cubic metals. The models are described in Ref. 9 and the underlying methodology is presented in Ref. 7. Here the mechanical response (load, stress, and transverse strain versus longitudinal strain) is determined on primary paths of uniaxial loading coaxial with the principal symmetry directions, i.e., [100], [110], and [111]. Also the locations of potential instabilities on the [100] paths at the ''$C_{22}=C_{23}$ eigenstates[16–18]'' are determined; the occurrence and positions of these states on the [100] paths profoundly affect the [110] paths, since the latter branch from the former, under strict uniaxial load, at branch points coincident with the eigenstates. Additional physical phenomena influenced by the path branchings are stress-induced phase transitions, which may be prevalent when the $C_{22}=C_{23}$ states lie at relatively low stresses (as in the alkali metals),[5,6] and crack propagation and dislocation emission from a crack tip.[26] Subsequent papers will deal specifically with the issues of stability under load and the detailed nature of path branchings.

Three general characteristic elastic responses are observed among the cubic metals, i.e., those of the fcc metals, the bcc alkali metals, and the bcc group-V and group-VI transition metals. These are displayed and explained systematically. First the mechanical response of Cu is examined, as a representative of fcc metals; this is followed by expositions of the response of a representative bcc alkali metal (Na) and of a typical bcc transition metal (Mo). In order to emphasize the role of structure, as distinct from bonding, the behavior of fcc Na is also presented and contrasted with that of bcc Na; in the fcc configuration, the mechanical response of Na is similar to that of other fcc metals, although as indicated above, the $C_{22}=C_{23}$ eigenstate occurs at a relatively low stress (and strain) on the [100] path. The influence of bonding character, as distinct from structure, is seen from comparing bcc Na and Mo. For example, strong, noncentral, directional bonding evidently causes the magnitude of the uniaxial stress in Mo, at a given small (but finite) longitudinal strain, to be greatest under [100] loading and least under [111] loading, whereas the opposite occurs in bcc Na. The behavior of Mo is somewhat contrary to intuition; i.e., one might expect the stress magnitude to be greatest along the ''close-packed'' [111] direction. (Consider, e.g., if the atoms were incompressible ''hard spheres,'' then the compressive stress, at finite strain, under a [111] load, would be infinite.) However, under large strain, the uniaxial compressive stress in Mo does become greatest along the [111] direction, as expected. Analogously, the [110] stress magnitude in fcc metals also becomes greatest under high compression. (The necessary ordering of the uniaxial stresses σ_{hkl} along the $[hkl]$ directions must be either $\sigma_{100}\geqslant\sigma_{110}\geqslant\sigma_{111}$ or $\sigma_{111}>\sigma_{110}>\sigma_{100}$ for cubic crystals under *infinitesimal* strain, according to general elasticity requirements,[15] although neither of these orderings need be observed under finite strain.)

Numerous comparisons are made among the qualitative and quantitative theoretical responses of the three ''normal'' metals, Cu, Na, and Mo, and of an ''anomalous'' metal, Al; these lead to various insights into the influence of crystal symmetry, bifurcation, and bonding character upon mechanical response, as is discussed in detail in the prior section. After thoroughly discussing the mechanical responses of these four metals, numerical values indicative of the responses of all twelve metals are listed and evaluated. Favorable comparisons are made among computed ''theoretical strengths'' and experimental whisker strengths. This is of broad interest, since a common goal of metal physicists, materials scientists, and metallurgists is to design and create strong metals. The strength of metals is of course ultimately limited by the strength inherent in the atomic bonds and the ability of the metal to remain stable under load. Metals used in most structural applications are in ''bulk form,'' and the strengths are much lower than those computed here or than those of fine metallic whiskers, owing to the presence of various defects in the bulk. In brittle metals, microcracks and other stress raisers cause localized stresses that greatly exceed the average stress present in the bulk. In such cases, failure generally occurs by crack propagation, and the highly localized stresses in the neighborhood of the crack tip may approach those inherent in the strength of the bonds. In ductile metals, dislocations readily glide on slip planes in the presence of much lower stresses, causing permanent deformation of the bulk. The strength of ductile metals can be enhanced by the ''pinning'' of dislocations, generally against precipitates, grain boundaries, or other dislocations, thus rendering them immobile. Here again, highly localized stresses,

approaching the inherent bond strengths, may be built up in the neighborhood of such ''pinning sites.'' The reasonably good agreement between calculated and experimental whisker strengths apparently is owing to the very large stress required to nucleate and/or propagate a dislocation in such fine structural specimens.

Estimates of the theoretical strength of crystals are often stated as a percent of the initial Young's modulus, without accounting for anisotropic crystalline effects. Here the influence of crystal structure and bifurcation phenomena is further elucidated from comparisons of the normalized uniaxial loading curves σ_a/E vs λ_a, where the axial stress $\sigma_a \equiv \sigma_{hkl}$, the initial Young modulus $E \equiv E_{hkl}$, and the longitudinal stretch $\lambda_a \equiv \lambda_{hkl}$; the inadequacy of simply quoting a theoretical strength as a percent of E, without reference to the specific structure and the mode of loading, is clearly demonstrated for a wide variety of metals. For example, among bcc metals, the maximum tensile stress in [100] loading ranged from about 1% (for Li) to 7.5% (for Nb) of E_{100}, whereas in [110] loading, the maximum stress varied from about 16% (for Fe) to 35% (for Na) of E_{110}. By contrast, among fcc metals (excluding Al), the maximum tensile stresses encompass values from 1.6% (for Na) to 5% (for Ni) of E_{110} under [110] loading and from 28% (for Ni) to 100% (for Na) of E_{100} under [100] loading. The response of the alkali metals is particularly anisotropic at finite strain.

Finally, connections are made with the present theoretical, finite strain, elastic responses of metals and the crack propagation simulations of Ref. 26, and comparisons are made among our results and those of earlier studies based on a simpler, central-force, model of crystals. The comparisons show that the central-force model (which ''captures the essence of atomic bonding,'' i.e., interatomic interactions that are repulsive and attractive, respectively, at small and large interatomic distances) yields good qualitative agreement with the present results for fcc metals and the bcc alkali metals. However, a more sophisticated approach, as is used in the present study, is required to model even qualitatively the anisotropic response of the group-V and group-VI bcc transition metals.

ACKNOWLEDGMENTS

We wish to acknowledge the support of the Campus Laboratory Collaborations Program of the University of California and to thank Ryan Lotz for his valuable assistance.

*Present address: King Mongkut's University of Technology Thonburi, Bangkok 10140, Thailand.

[1] D. A. Young, *Phase Diagrams of the Elements* (Univ. of California, Berkeley, 1991).
[2] R. J. Gooding, Y. Y. Ye, C. T. Chan, K. M. Ho, and B. N. Harmon, Phys. Rev. B **43**, 13 626 (1991).
[3] J. Wang, S. Yip, S. R. Phillpot, and D. Wolf, Phys. Rev. Lett. **71**, 4182 (1993).
[4] E. Kaxiras and L. L. Boyer, Phys. Rev. B **50**, 1535 (1994).
[5] F. Milstein, J. Marschall, and H. E. Fang, Phys. Rev. Lett. **74**, 2977 (1995).
[6] C. Maier, O. Blaschko, and W. Pichl, Phys. Rev. B **55**, 12 062 (1997).
[7] S. Chantasiriwan and F. Milstein, Phys. Rev. B **48**, 14 080 (1996).
[8] M. S. Daw, S. M. Foiles, and M. I. Baskes, Mater. Sci. Rep. **9**, 251 (1993).
[9] S. Chantasiriwan and F. Milstein, preceding paper [Phys. Rev. B **58**, 5996 (1998)].
[10] R. Hill, Math. Proc. Camb. Philos. Soc. **77**, 225 (1975).
[11] F. Milstein and K. Huang, Phys. Rev. B **19**, 2030 (1979).
[12] F. Milstein and D. J. Rasky, Philos. Mag. A **45**, 49 (1982).
[13] F. Milstein and J. Marschall, Philos. Mag. A **58**, 365 (1988).
[14] K. Kitagawa, M. Veda, and H. Miyamoto, Acta Metall. **28**, 1505 (1980).
[15] F. Milstein and J. Marschall, Acta Metall. Mater. **40**, 1229 (1992).
[16] R. Hill and F. Milstein, Phys. Rev. B **15**, 3087 (1977).
[17] F. Milstein and B. Farber, Phys. Rev. Lett. **44**, 277 (1980).
[18] F. Milstein, in *Mechanics of Solids*, edited by H. G. Hopkins and M. J. Sewell (Pergamon, Oxford, 1982), pp. 417–452.
[19] M. Born, Proc. Cambridge Philos. Soc. **36**, 160 (1940).
[20] M. Born and R. Fürth, Proc. Cambridge Philos. Soc. **36**, 454 (1940).
[21] R. Fürth, Proc. Cambridge Philos. Soc. **37**, 177 (1941).
[22] F. Milstein and R. Hill, J. Mech. Phys. Solids **27**, 255 (1979).
[23] F. Milstein and R. Hill, Phys. Rev. Lett. **43**, 1411 (1979).
[24] R. Hill, Math. Proc. Camb. Philos. Soc. **92**, 167 (1982).
[25] F. Milstein, H. E. Fang, X. Y. Gong, and D. J. Rasky, Solid State Commun. **99**, 807 (1996).
[26] F. Abraham (unpublished); a partial account appears in a ''note added in proof'' in F. F. Abraham, D. Schneider, B. Land, D. Lifka, J. Skovira, J. Gerner, and M. Rosenkrantz, J. Mech. Phys. Solids **45**, 1461 (1997).
[27] B. P. J. Sandvik and C. M. Wayman, Metall. Trans. A **14**, 835 (1983).
[28] F. Milstein, H. E. Fang, and J. Marschall, Philos. Mag. A **70**, 621 (1994).
[29] F. Milstein and B. Farber, Philos. Mag. A **42**, 19 (1980).
[30] A. Kelly, *Strong Solids*, 2nd ed. (Clarendon, Oxford, 1973).
[31] S. S. Brenner, J. Appl. Phys. **27**, 1484 (1956).
[32] F. Milstein, R. Hill, and K. Huang, Phys. Rev. B **21**, 4282 (1980).
[33] F. Milstein, Phys. Rev. B **2**, 512 (1970).
[34] F. Milstein, Phys. Rev. B **3**, 1130 (1971).
[35] F. Milstein, J. Appl. Phys. **44**, 3825 (1973).
[36] F. Milstein, J. Appl. Phys. **44**, 3833 (1973).